Nationaal Lucht- en Ruimtevaartlaboratorium
National Aerospace Laboratory NLR

NLR-TP-98235

2D Maximum lift prediction of a three element airfoil

K.M.J. de Cock

Nationaal Lucht- en Ruimtevaartlaboratorium
National Aerospace Laboratory NLR

NLR-TP-98235

2D Maximum lift prediction of a three element airfoil

K.M.J. de Cock

This investigation has been carried out under a contract awarded by the Netherlands Agency for Aerospace Programmes (NIVR), contract number 01308N.
NIVR has granted NLR permission to publish this report.

This report is based on a presentation held at the Symposium on Computational and Experimental Methods in Mechanical and Thermal Engineering, May 7-8, 1998, University of Gent, Belgium.

Division:	Fluid Dynamics
Issued:	September 1998
Classification of title:	unclassified

Abstract

In this paper the 2D maximum lift prediction capability of an unstructured Reynolds-Averaged Navier-Stokes (RANS) CFD method is evaluated. The Fully Automatic Navier-Stokes (FANS) method is briefly described. 2D maximum lift for a three element airfoil is predicted and compared with experiments, for both take-off and landing. The conclusion of this evaluation is that the present RANS CFD method, based on the k-ω turbulence model, gives an adequate predictive capability of maximum lift for the take-off configuration, including a significant confluence between slat wake and wing boundary layer. For the landing configuration, the CFD method predicts the shape of the lift curve and angle of attack at maximum lift. The deficiency in the maximum lift prediction for the landing configuration is due to the absense of an extra rate-of-strain term in the k-ω turbulence model.

Contents

15 Figures

(22 pages in total)

1 Introduction

High-lift devices such as a typical three element airfoil depicted in figure 1 are installed on aircraft wings in order to generate an increased maximum lift coefficient of the wing during take-off and landing.

An important topic in the final design of the high-lift device is the accurate prediction of the maximum lift coefficient that can be obtained with a given configuration, and the pitching moment characteristic. For take-off conditions drag is also an important characteristic, at least for two-engine aircraft.

The problem of maximum lift prediction is challenging for both experiments and CFD due to the mix of complex flow phenomena involved such as transition, separation, low subsonic flow combined with transonic flow (on the slat), wake-boundary layer confluence, etc.

Up to now, accurate 3D maximum lift prediction based on the Reynolds-Averaged Navier-Stokes (RANS) is not yet feasible. For this reason, this paper will be restricted to 2D maximum lift prediction for a three element airfoil.

In order to accurately predict 2D maximum lift, the CFD method should be capable to capture the relevant flow mechanisms causing maximum lift, and in order to be practical, this prediction should be available within a short turn-around time.

In this paper the 2D maximum lift prediction capability of an unstructured Reynolds-Averaged Navier-Stokes (RANS) CFD method is evaluated.

2 FANS, a 2D CFD method for maximum lift prediction

FANS (Fully Automatic Navier-Stokes method) is a 2D CFD method, primarily developed for accurate high-lift flow simulations within short turn-around times.

2.1 Grid generation

In figure 2 a flow diagram is given for the automatic generation of high quality, unstructured viscous flow grids within FANS. Starting point is the input geometry defined in terms of curves (which are given by there support points). The input geometry usually has regions where the first and/or second derivative behaves singular (for instance at the trailing edge of an airfoil).

In the first step, the input geometry is automatically preprocessed, resulting in a regularized geometry and a boundary conforming geometry, see figure 3.

In the next step, an Euler grid is generated around the boundary conforming geometry, based on user specified maximum spacings and curvatures. The Euler grid generation algorithm is of the quadtree type, see reference 2.

Finally, a viscous flow grid with high aspect ratio grid cells is introduced between the regularized geometry and the boundary conforming geometry, based on the (user-specified) number of grid points across the boundary conforming region, reference 3.

The resulting viscous flow grids have a number of important properties : smoothness (both spatial and topological) and central symmetry in the viscous flow region, see also reference 1. Provided a special definition of the control volumes in the flow solver is used (avoiding degeneration of the control volume for high aspect ratio viscous flow grids), accurate viscous flow solutions can be obtained on these grids.

A detail of the high aspect ratio viscous flow grid between the wing and slat is given in figure 4.

2.2 Flow solver

The Reynolds-Averaged Navier-Stokes equations for compressible flow are solved, coupled with a standard k-ω turbulence model.

This k-ω turbulence model is fixed for a number of known problems : regions of laminar flow can be enforced in the boundary layer part of the grid, a background production term is introduced to allow the simulation of a free stream with a uniform low turbulent Reynolds number, wall

roughness effects are introduced via the solid wall boundary condition for ω, and the production terms are modified according to ref. 6 to avoid an excess of turbulent production near stagnation zones. The SST modification of the k-ω turbulence model introduced in the latter reference is not implemented in FANS.

Polynomial upwind flux-difference splitting according to ref. 4 is used for discretizing the convective flux, in combination with a central discretization of the viscous flux, ref. 8. Second order spatial accuracy is obtained by the MUSCL approach for all equations, applying a smooth version of the Barth-Jespersen limiter, references 5 and 11.

The source terms of the turbulence model are treated in a point implicit manner.

The discretized equations are solved with a defect correction multigrid method.

For 2D maximum lift prediction typically a chain of computations for subsequent angles of attack are made overnight, see fig. 5. The lift coefficient as well as the drag coefficient level off for each angle of attack (landing, case b01, ..., b07).

For the remaining cases b08, b09 and b10, the chain of computations broke down because the specified transition onset locations of case b01, ..., b07 became unrealistic on the slat and flap upper surface. This aspect of transition onset location definition is critical for short turn around time 2D maximum lift prediction.

Maximum lift itself can be very sensitive to the extent of laminar flow, even at high, full scale flight Reynolds numbers. Unrealistic transition onset locations generally destroy the accuracy of the maximum lift prediction (both the maximum lift level and angle of attack). For instance, take-off maximum lift due to slat separation instead of wing separation is found if the slat transition onset locations are specified too far downstream.

3 Take-off maximum lift prediction

The take-off configuration of the three element airfoil considered here can be characterized by moderate slat and flap settings (a low drag coefficient is important during take-off, hence massive separations should be avoided by moderate slat and flap settings).

Both the take-off and landing case have been extensively tested within GARTEUR Action Group AD(AG08) in the NLR transonic wind tunnel HST. These experimental results (described in more detail in references 9 and 10) are used in this paper, for free stream Mach and Reynolds numbers of 0.2 and 4 million respectively.

In figure 6 a comparison is made for the take-off configuration between the lift coefficients of both the experiments and CFD computations (case a01 upto a10, for increasing angle of attack). The agreement between experiments and CFD computations can be qualified as very good although the computations give a slightly higher maximum lift coefficient. The slat, wing and flap pressure coefficient distributions match very well, figure 10, 12 and 14 for both a low and high angle of attack (the latter at maximum lift).

In figure 8 the computed wing upper surface skin friction is shown. It can be observed from this figure that separation occurs first on the wing upper surface, near the trailing edge, which is also the case in the experiments.

It can be concluded that for take-off (no massive separations), the relevant flow mechanisms (including significant confluence between the slat wake and the wing boundary layer) responsible for reaching maximum lift, can be well predicted even with a standard k-ω turbulence model, provided that transition onset onset locations are realistically specified.

4 Landing maximum lift prediction

The landing configuration of the three element airfoil is characterized by more extreme slat and flap settings. The free stream Mach and Reynolds numbers are 0.2 and 4 million respectively.

In figure 7 a comparison is made between the integrated lift coefficients of both the experiments and CFD computations. Both the shape of the curve and the angle of attack for which maximum lift is reached are reproduced. Unsteady flow is found beyond maximum lift, cases b09 and b10.

The lack of agreement between the experimental and CFD maximum lift value is larger than for take-off, the computations giving a lift curve that is shifted to a higher lift level. This can also be observed from the slat, wing and flap pressure coefficient distributions, figures 11, 13 and 15, with lower computed suction side pressure coefficients compared to the experiments (scales correspond to figures 10, 12 and 14). The shift in the lift curve is directly related to the fact that the experimentally observed separation on the flap upper surface (for low angles of attack) is not found in the computations.

These differences between the CFD results and the experimental data for the landing configuration can be largely attributed to the inadequate response of a standard k-ω turbulence model to the higher adverse pressure gradients in the landing case (which are leading to higher boundary layer loads, and higher "off-the-surface" pressure recovery in the wakes), see reference 7. Improvement of the turbulence model by the introduction of the effect of extra strain rates on the turbulent shear stress can be conducted following the lines of references 6 or 7.

Remark that the large separation on the flap, present for low angles of attack, disappears close to maximum lift, resulting in a better CFD prediction of the shape of the flap pressure coefficient distribution.

At maximum lift for the landing configuration, the slat starts to separate near the leading edge, see figure 9, resulting in a discontinuous change of the lift coefficient. This mechanism is reproduced by the CFD computations, resulting in a correct shape of the predicted lift curve and the correct maximum lift angle of attack. The difference in stalling mechanism between the take-off and landing configuration (wing trailing edge versus slat leading edge) is reflected in the different change of the lift coefficient beyond maximum lift, compare figures 6 and 7.

5 Conclusions

The CFD method gives an very good prediction of the maximum lift for the take-off configuration of the three element airfoil studied. The pressure coefficient as well as the mechanism responsible for maximum lift and the maximum lift angle of attack are in very good agreement with the experimental data.

For the landing configuration, the CFD method properly predicts both the shape of the lift curve and the maximum lift angle of attack. The agreement between the experimental and CFD maximum lift value is less good than for take-off, due to the inadequate response of a standard k-ω turbulence model to the higher adverse pressure gradients of the landing configuration.

For both the take-off and landing case, a realistic and automatic definition of the transition onset locations on the lower and upper surfaces of the three element airfoil is crucial for a short turn-around time and high accuracy of the 2D maximum lift prediction.

6 Acknowledgements

The three element airfoil HST wind tunnel results are obtained within GARTEUR Action Group AD(AG08).

Computations presented in the paper are conducted within the NLR participation to the GARTEUR Action Group AD(AG25) "2D maximum lift prediction".

Dr. B. Oskam is thanked for carefully reading this paper.

7 References

1. T.J. Baker, 'Irregular meshes and the propagation of solution errors', proceedings of the 15th Int. Conf. on Num. Methods in fluid dynamics, (1996)
2. K.M.J. de Cock, 'High-lift system analysis method using unstructured meshes', NLR TP 92351 (1992)
3. K.M.J. de Cock, 'Fully automatic Navier Stokes algorithm for 2D high-lift flows', NLR TP 96487 (1996)
4. E. Dick, 'A flux-difference splitting method for steady Euler equations', J. Comp. Phys., 76, pag. 19-32 (1988)
5. B. van Leer, 'Towards the ultimate conservation difference scheme V, a second order sequel to Godunov's method', J. Comp. Phys., 32, pag 101-136, (1979).
6. F.R. Menter, 'Zonal two equation k-ω turbulence models for aerodynamic flows', AIAA-93-2906 (1993)
7. B. Oskam and D.J. Laan and D.F. Volkers, 'Recent advances in computational methods to solve the high-lift multi-component airfoil problem', NLR MP 84042, 1984.
8. J. Steelandt and E. Dick, 'A multigrid method for the compressible Navier-Stokes equations coupled to the k-ϵ equations', International journal of numerical methods for heat and fluid flow (1994)
9. A.P.P. Termes, 'Reynolds and Mach number effects and 2D-3D correlation based on measurements and computed results for the GARTEUR take-off configuration', NLR TP 95106 (1994)
10. J.J. Thibert, 'The GARTEUR high-lift programme', AGARD conference proceedings 515 (1992)
11. V. Venkatakrishnan, 'Convergence to steady state solutions of the Euler equations on unstructured grids with limiters', J. Comp. Phys., 118, pag. 120-130 (1995)

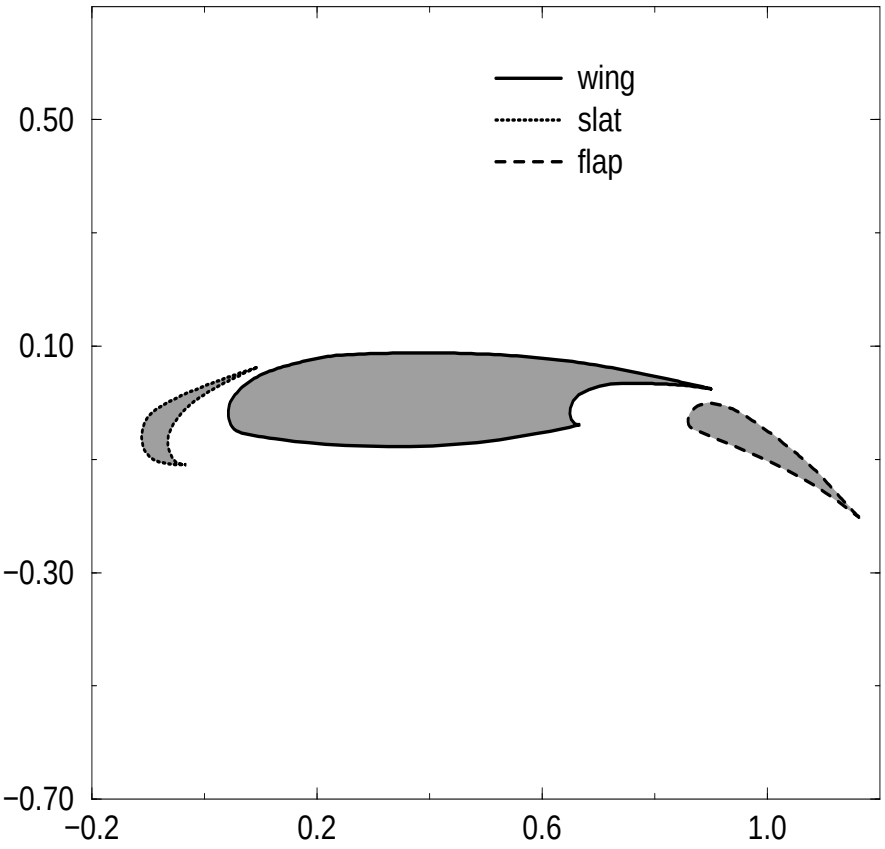

Fig. 1 Generic three element airfoil

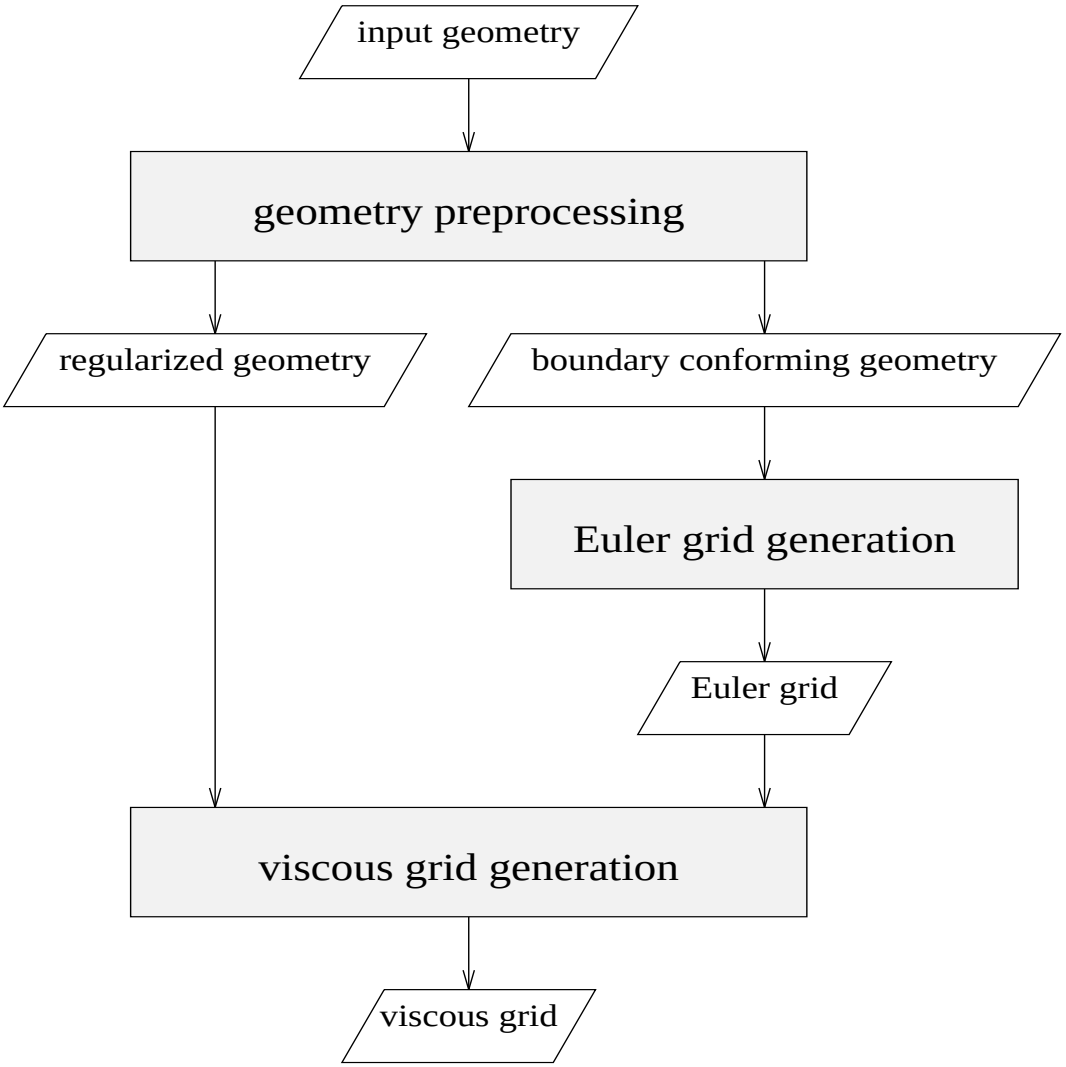

Fig. 2 Grid generation flow diagram

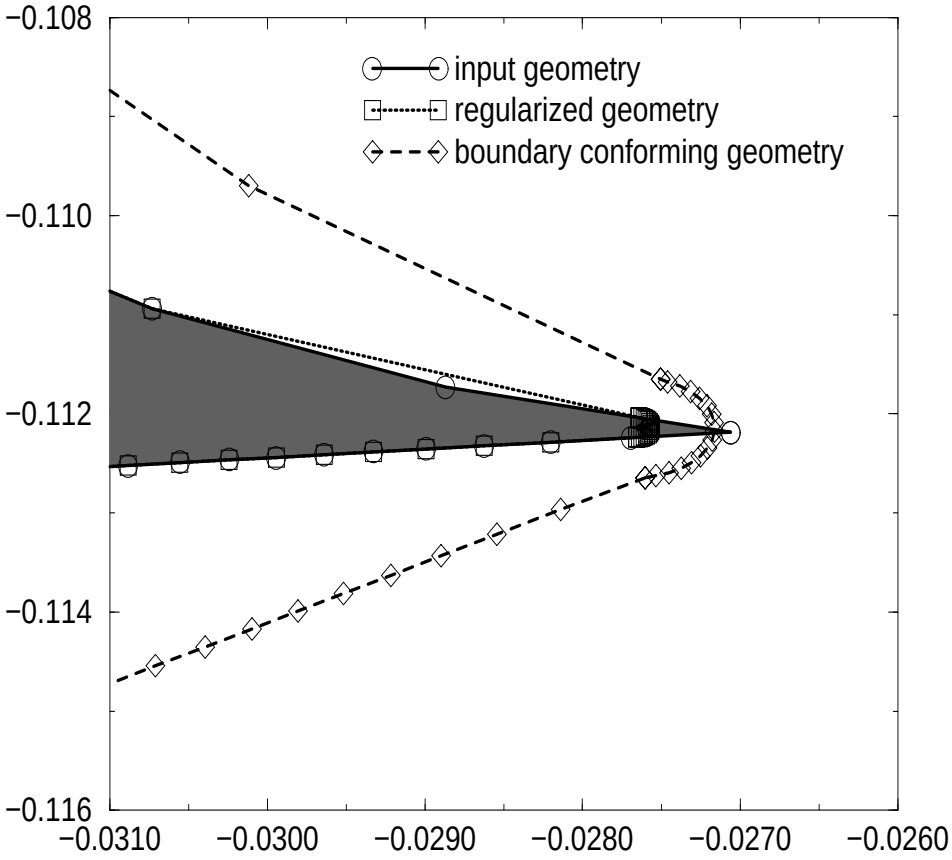

Fig. 3 Input, regularized and boundary conforming geometries around the slat hook

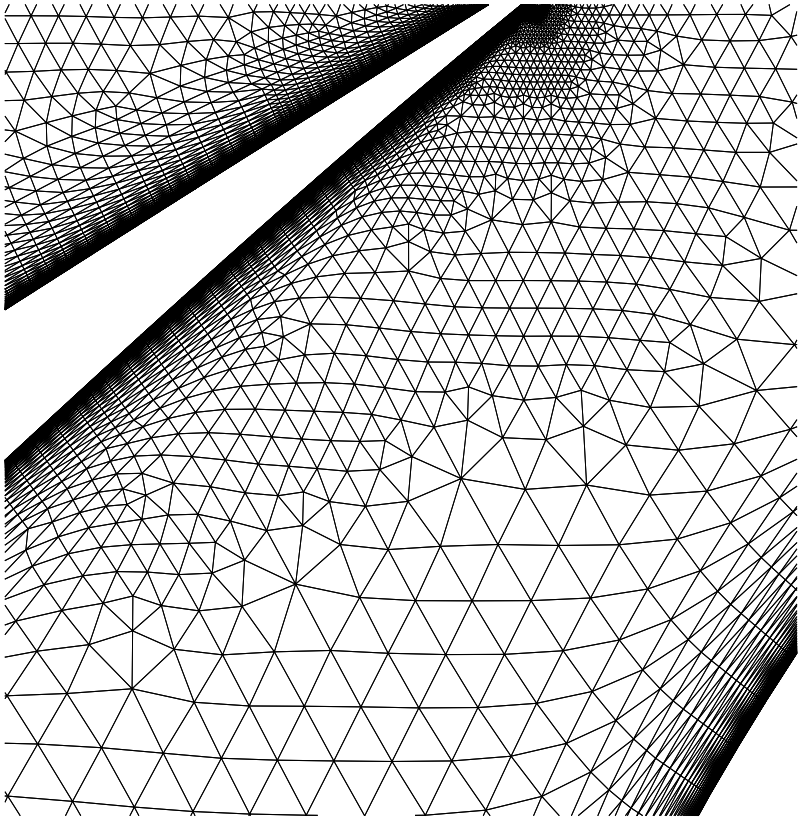

Fig. 4 Detail of high aspect ratio viscous flow grid between wing and slat

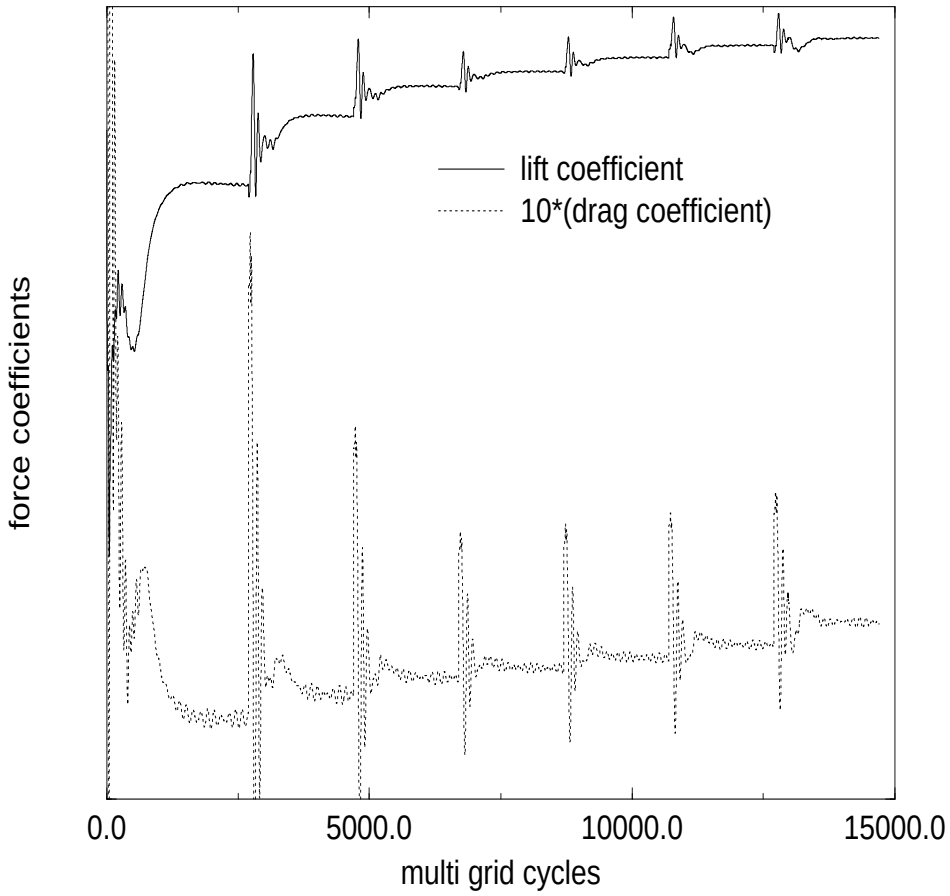

Fig. 5 Lift and drag coefficient history (landing, 7 angles of attack b01, ..., b07)

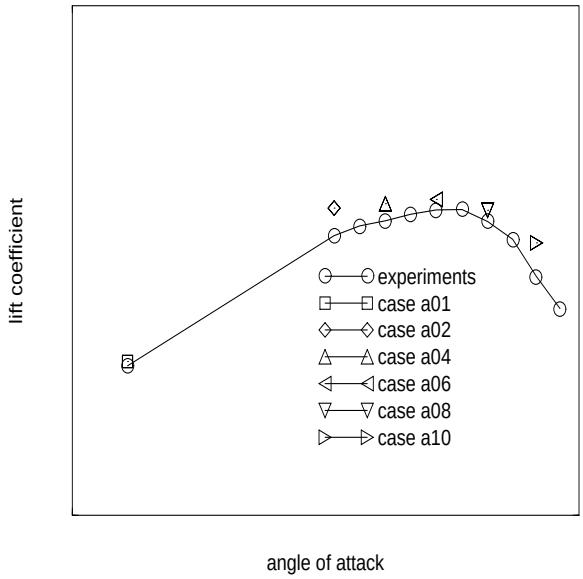

Fig. 6 Three element airfoil in take-off configuration (Mach = 0.2, Re = 4 million, available HST transition locations are used) : lift coefficient vs. angle of attack (same scales as fig. 7)

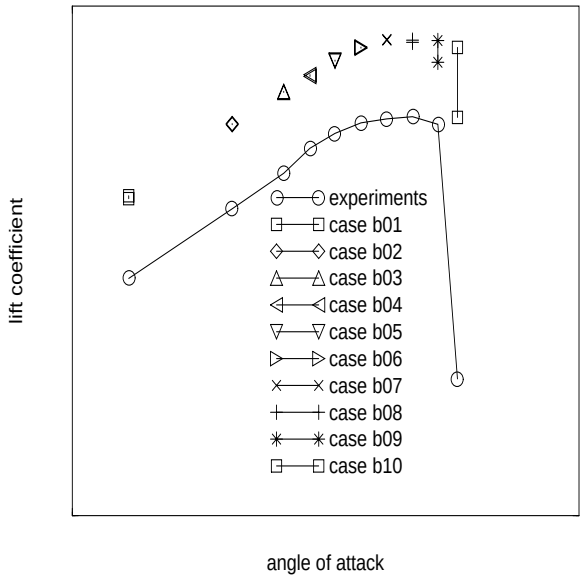

Fig. 7 Three element airfoil in landing configuration (Mach = 0.2, Re = 4 million, available HST transition locations are used) : lift coefficient vs. angle of attack (same scales as fig. 6)

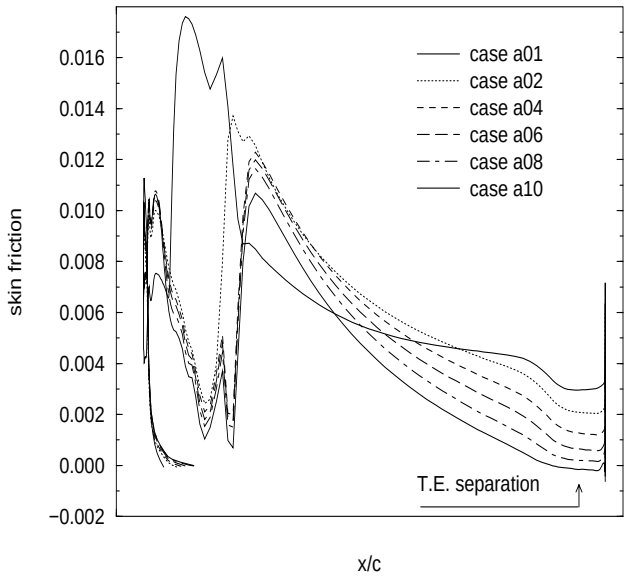

Fig. 8 Three element airfoil in take-off configuration (Mach = 0.2, Re = 4 million) : wing upper surface skin friction coefficient vs. x/c. Remark the wing trailing edge separation for case a10

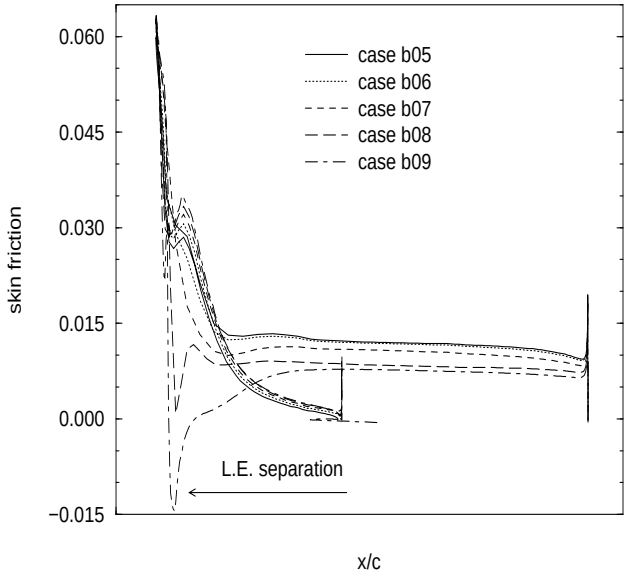

Fig. 9 Three element airfoil in landing configuration (Mach = 0.2, Re = 4 million) : slat upper surface skin friction coefficient vs. x/c. Remark the slat leading edge separation for case b09

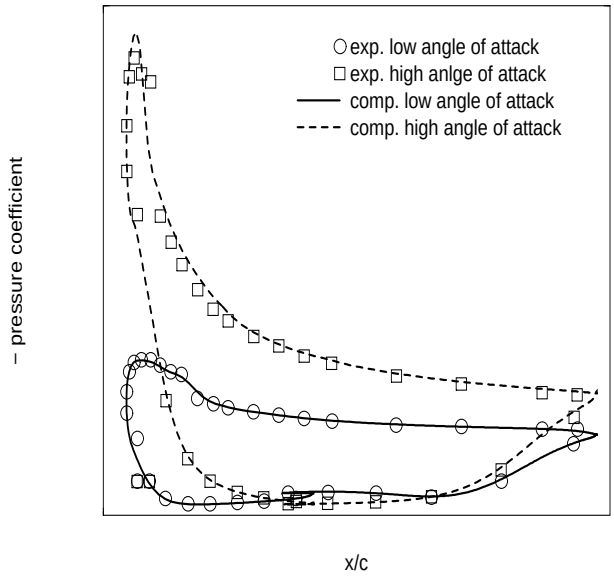

Fig. 10 Three element airfoil in take-off configuration (Mach = 0.2, Re = 4 million) : slat pressure coefficient vs. x/c (low vs. high angle of attack)

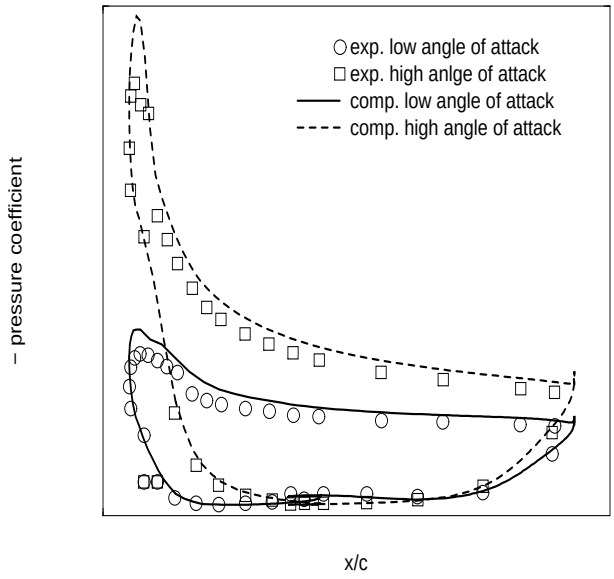

Fig. 11 Three element airfoil in landing configuration (Mach = 0.2, Re = 4 million) : slat pressure coefficient vs. x/c (low vs. high angle of attack)

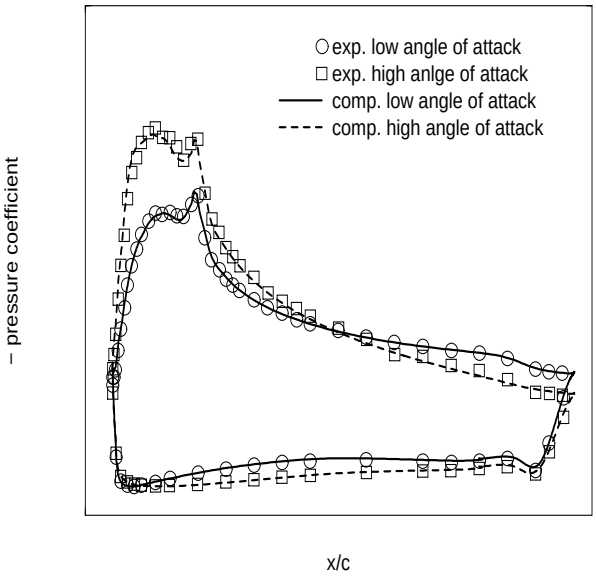

Fig. 12 Three element airfoil in take-off configuration (Mach = 0.2, Re = 4 million) : wing pressure coefficient vs. x/c (low vs. high angle of attack)

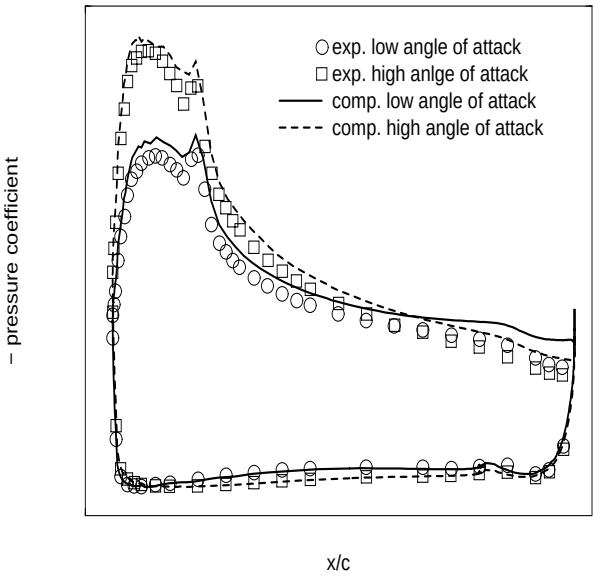

Fig. 13 Three element airfoil in landing configuration (Mach = 0.2, Re = 4 million) : wing pressure coefficient vs. x/c (low vs. high angle of attack)

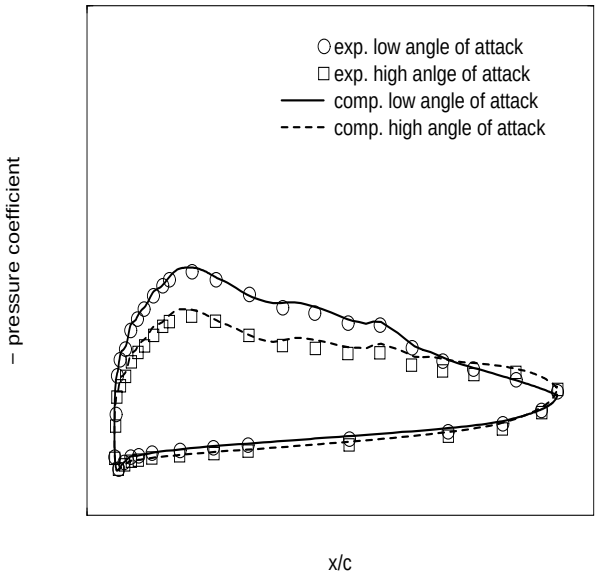

Fig. 14 Three element airfoil in take-off configuration (Mach = 0.2, Re = 4 million) : flap pressure coefficient vs. x/c (low vs. high angle of attack)

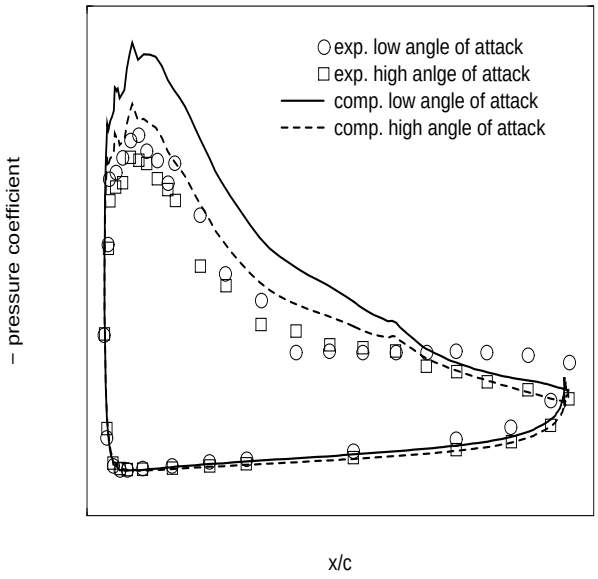

Fig. 15 Three element airfoil in landing configuration (Mach = 0.2, Re = 4 million) : flap pressure coefficient vs. x/c (low vs. high angle of attack)